Solar Energy Materials and Solar Cells 174 (2018) 405–411

Contents lists available at ScienceDirect

Solar Energy Materials and Solar Cells

journal homepage: www.elsevier.com/locate/solmat

Colloidal quantum dot solar cell electrical parameter non-destructive quantitative imaging using high-frequency heterodyne lock-in carrierography and photocarrier radiometry

Lilei Hu[a], Mengxia Liu[b], Andreas Mandelis[a,b,*], Qiming Sun[a], Alexander Melnikov[a], Edward H. Sargent[b]

[a] Center for Advanced Diffusion-Wave and Photoacoustic Technologies (CADIPT), Department of Mechanical and Industrial Engineering, University of Toronto, Toronto, Ontario, Canada, M5S 3G8

[b] Edward S. Rogers Sr. Department of Electrical and Computer Engineering, University of Toronto, Toronto, Ontario, Canada, M5S 3G4

ARTICLE INFO

Keywords:
Colloidal quantum dots (CQDs)
Solar cell
Carrier transport dynamics
Trap states
Carrier lifetime
Large-area imaging

ABSTRACT

Colloidal quantum dot (CQD) solar cells with a certified power conversion efficiency of 11.28% were characterized using camera-based heterodyne lock-in carrierography (HeLIC) and photocarrier radiometry (PCR). Carrier lifetime, diffusivity, and diffusion and drift length of a CQD solar cell were imaged in order to investigate carrier transport dynamics, as well as solar cell homogeneity and the effects of Au contacts on carrier transport dynamics. Using room temperature HeLIC imaging which has also been demonstrated using PCR measurements, shorter carrier lifetimes (ca. 0.5 μs) were found in Au contact regions that can be attributed to enhanced non-radiative recombinations through trap states at Au/CQD interfaces. This imaging methodology shows strong potential for elucidating the energy loss physics of CQD solar cells and for industrial non-destructive large-area photovoltaic device characterization.

1. Introduction

Colloidal quantum dots (CQDs) with tunable bandgap through effective control over CQD sizes have become promising candidates for fabricating low-cost, large-area, flexible, and lightweight solar cells [1–6]. Although CQD solar cell efficiencies have been boosted to 13.4% [7], there is still space for further improvement for commercial applications. Therefore, understanding of CQD solar cell energy loss mechanisms through factors such as film/contact interfaces [2,8], inefficient electrode collection of carriers [2,6], various trap states [9–12], CQD size polydispersity [13–15], and CQD bandtail states which deteriorate open-circuit voltage and inhibit carrier transport [1,6], is necessary for future photovoltaic device optimization.

Nowadays, large-area photovoltaic solar cells prevail, the characterization of which fulfills various purposes including shading effects, fundamental carrier transport dynamics, mechanical and electrical defect evaluation. Therefore, large-area characterization methodologies are needed for CQD solar cell efficiency optimization. Spatially resolved photoluminescence (PL) and electroluminescence (EL) constitute powerful methodologies for the characterization of silicon wafers [16–18] and solar cells [18–21]. They yield measurements of minority carrier hopping lifetime [16,17,20], open-circuit voltage [18,20,21], current density [21], series resistance [21], fill factor [18,21], and quality monitoring in different device fabrication steps [19]. Furthermore, due to the high signal-to-noise ratio (SNR), synchronous frequency-domain imaging methodologies are emerging, such as the lock-in thermography (LIT) [22] that has been used for determining series resistance and recombination current at a frequency of 20 Hz. However, static (dc) PL and EL, and low-frequency LIT limited by the low camera frame rate, cannot monitor electronic transport kinetics and recombination dynamics. The latter, however, are key parameters for the determination of photovoltaic energy conversion and dissipation.

To address these critical issues, here we introduce single detector-based photocarrier radiometry (PCR), and camera-based homodyne (HoLIC) and heterodyne (HeLIC) lock-in carrierographies for the characterization CQD solar cells. HoLIC imaging and PCR are the same type of dynamic spectrally gated frequency-domain photoluminescence modality and can yield quantitative information about carrier transport dynamics with accuracy and precision superior to the time-resolved PL due to their intrinsically high signal-to-noise ratio (SNR) by virtue of

* Corresponding author at: Center for Advanced Diffusion-Wave and Photoacoustic Technologies (CADIPT), Department of Mechanical and Industrial Engineering, University of Toronto, Toronto, Ontario, Canada, M5S 3G8.
E-mail address: mandelis@mie.utoronto.ca (A. Mandelis).

http://dx.doi.org/10.1016/j.solmat.2017.09.020
Received 26 April 2017; Received in revised form 29 July 2017; Accepted 11 September 2017

lock-in demodulation [23,24]. HoLIC has advantages as an all-optical non-destructive imaging technique for large-area photovoltaic device imaging, yet it is limited to the low modulation frequency range (< 1 kHz) due to the low frame rates of conventional cameras [25]. Using a single InGaAs detector, PCR can attain high-frequency characterization (> 100 kHz), however, the fast large-area imaging capability is compromised. Through creating a slow enough beat frequency component, HeLIC overcomes the high-frequency limitation of conventional camera-based optical characterization techniques and the poor SNR at short exposure times associated with high frame rates [26] to realize frequency-modulated imaging at more than 100 kHz. Therefore, with higher SNR than dc PL imaging, HeLIC can attain a wide range of frequency-dependent ac carrier diffusion lengths to generate depth-selective/resolved high-frequency imaging of carrier transport parameters in large-scale devices. It should be noted that all three techniques (PCR, HoLIC, and HeLIC) have no low-frequency limitations.

Therefore, to study carrier transport dynamics in CQD solar cells and the effects of CQD layer inhomogeneity (for example, induced at various fabrication stages) and contact/film interface effects on solar cell performance, we combined a *J-V* model with PCR and HeLIC to quantitatively produce carrier lifetime, diffusivity, and drift and diffusion length images for a high-efficiency CQD solar cell under frequency modulated excitation. This methodology has a strong potential impact on solar cell efficiency optimization and on industrial non-destructive solar cell quality control.

2. Theoretical methods

2.1. Solar cell under harmonic excitation

The nature of photocarrier generation, discrete hopping transport, and recombination in CQD-based thin films was found to follow a hopping diffusion transport behavior [2,27] under frequency-modulated laser excitation that reveals details of carrier hopping transport dynamics in these photovoltaic materials. Here, in order to extract charge carrier hopping transport dynamics in CQD-based solar cells Fig. 1(a), light-matter interaction under modulated-frequency excitation is investigated as an extension of conventional current-voltage characterization of CQD solar cells under dc laser excitation [2,6,28]. Reviewing the CQD solar cell structure in Fig. 1, due to the larger bandgap energy of ZnO than the incident excitation photon energy and the thicker CQD layers than ZnO, charge carriers and excitons are considered to be generated only in CQD layers, thus contributing to the primary current within this type of solar cell. In a manner similar to the carrier hopping transport model under static excitation [2], as electrons are injected from CQD layer to the electron-accepting ZnO nanoparticles [1], the rate equation for electrons in the CQD layers under dynamic illumination can be written as

$$\frac{\partial \Delta n(x,t)}{\partial t} = \frac{\partial J_e(x,t)}{\partial x} - \frac{\Delta n(x,t)}{\tau} + g(x,t) \tag{1}$$

$\Delta n(x,t)$ is the excess electron density and $J_e(x,t)$ is the electron current flux; τ is the electron carrier lifetime, and $g(x,t)$ is the carrier generation rate. Considering that the ambipolar diffusion coefficient and mobility, $J_e(x,t)$ can be further defined by [29,30]

$$J_e(x,t) = D_e \frac{\partial \Delta n(x,t)}{\partial x} + \mu_e E \Delta n(x,t) \tag{2}$$

where D_e is the diffusivity, μ_e is the mobility, and E is the electric field (a constant value given as the difference between the external and intrinsic electric fields), Eq. (1) is reduced to a diffusion equation which can be solved using the Green function method and transferred to the frequency domain through a Fourier transformation [29]. Upon harmonic optical excitation, the photoexcited excess carrier distribution follows the Beer-Lambert Law:

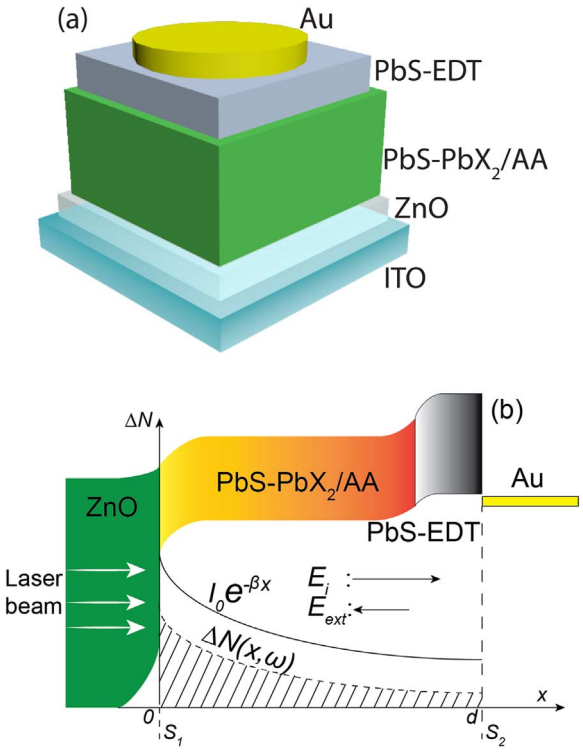

Fig. 1. Schematic of CQD solar cell sandwich structure (a), and the corresponding band energy structure (b) that shows the illumination depth profile, the photocarrier density wave distribution and the intrinsic and external electric fields.

$$g(x,\omega) = \frac{\beta \eta I_0}{2h\nu} e^{-\beta x}(1+e^{i\omega t}) \tag{3}$$

where β is the optical absorption coefficient, η is the quantum yield of the photogenerated carriers, and h and ν are the Plank constant and the frequency of incident photons, respectively. I_0 denotes the incident photon intensity. In the one-dimensional geometry, the boundary conditions at $x = 0$ and d, Fig. 1(b), can be written as functions of surface recombination velocities (S_1 and S_2 at $x = 0$ and $x = d$, respectively,) and the excess carrier density at the corresponding boundaries.

$$D_e \frac{\partial \Delta N(x,\omega)}{\partial x}\bigg|_{x=0} = S_1 \Delta N(0,\omega) \tag{4a}$$

$$-D_e \frac{\partial \Delta N(x,\omega)}{\partial x}\bigg|_{x=d} = S_2 \Delta N(d,\omega) \tag{4b}$$

where $\Delta N(x,\omega)$ is the Fourier transform $\Delta n(x,t)$, a carrier-density-wave (CDW). Therefore, the final expression of harmonic excess carriers $\Delta N(x,\omega)$ can be obtained as follows

$$\begin{aligned}\Delta N(x,\omega) = \frac{\eta I_0 \beta}{4h\nu D_e(1 - R_{e1}R_{e2}e^{-2K_e d})[\beta^2 - (Q_0^2 + \sigma_e^2)]}\{\big([(1+\rho_e) \\ - R_{e1}(1-\rho_e)] - R_{e1}[(\rho_e - 1) + R_{e2}(1+\rho_e)]e^{-(K_e+\beta)d}\big)e^{-K_e x} \\ + \big(R_{e2}[(1+\rho_e) - R_{e1}(1-\rho_e)] \\ + [(1-\rho_e) - R_{e2}(1+\rho_e)]e^{-(\beta-K_e)d}\big)e^{-K_e(2d-x)} \\ -2\big(1 - R_{e1}R_{e2}e^{-2K_e d}\big)e^{-\beta x}\}\end{aligned} \tag{5}$$

with the following definitions,

$$\overrightarrow{Q_0} = \frac{\mu_e}{2D_e}\overrightarrow{E}\ [\mathrm{cm}^{-1}]; \sigma_e = \sqrt{\frac{1+i\omega\tau}{D_e\tau}}\ [\mathrm{cm}^{-1}] \tag{6a}$$

$$R_{ej} = \frac{D_e\sqrt{Q_0^2 + \sigma_e^2} - S_j}{D_e\sqrt{Q_0^2 + \sigma_e^2} + S_j}, j = 1, 2 \tag{6b}$$